



**Abstract**

Observations show that equatorial ionospheric vertical drifts during solar minimum differ from the climatology between late afternoon and midnight. By analyzing WACCM-X simulations, which reproduce this solar cycle dependence, we show that the interplay of the dominant migrating tides, their propagating and in-situ forced components, and their solar cycle dependence impact the F-region wind dynamo. In particular, the amplitude and phase of the propagating migrating semidiurnal tide (SW2) in the F-region plays a key role. Under solar minimum conditions, the SW2 tide propagate to and beyond the F-region in the winter hemisphere, and consequently its zonal wind amplitude in the F-region is much stronger than that under solar maximum conditions. Furthermore, its phase shift leads to a strong eastward wind perturbation near local midnight. This in turn drives a F-region dynamo with an equatorial upward drift between 18-1 hour local times.

**Plain Language Summary**

The vertical ion motion in the equatorial ionosphere plays a key role in the space weather. Satellite observations found that such vertical motion during periods with low solar activity can be quite different from the known climatology, and the cause is not clear. Using a whole atmosphere general circulation model, WACCM-X, we are able to reproduce the pattern of the vertical ion motion similar to that observed during low activity solar cycle periods. By analyzing the model results, we find that the relative significance of the different atmosphere tidal wave components and its variation with solar activity contribute to the solar dependence of the vertical ion motion. The propagating altitudes of tide with 12-hour period, as well as where and when the tidal wind become large, are of particular importance.

**1 Introduction**

The ionospheric  $E \times B$  drift is a key quantity in ionospheric electrodynamics. In particular, the vertical component of  $E \times B$  drift at dusk and during night time can play a key role in the onset of F-region irregularities (Anderson et al., 2004; Fejer et al., 1999; Huang, 2018; Huang & Hairston, 2015; Kil et al., 2009). The vertical  $E \times B$  drift climatology, based on radar and satellite measurements, shows a clear seasonal variation and solar activity dependence (Scherliess & Fejer, 1999). The most significant variability is found in the vertical drift around dusk: strong pre-reversal enhancement (PRE) of the vertical drift often occurs around equinox and under more active solar conditions. The E and F regions dynamo and the the alignment of the geomagnetic field lines and the evening terminator are thought to be responsible for the PRE and its seasonal and solar activity dependence (Farley et al., 1986; Tsunoda, 1985). Fesen et al. (2000) simulated PRE and its seasonal and solar activity dependence using the Thermosphere/Ionosphere/Electrodynamic General Circulation Model (TIEGCM), and found that the E-region migrating semi-diurnal tide (SW2) plays an important role. The seasonal and solar activity dependence of PRE is recently simulated by the Whole Atmosphere Community Climate Model with thermosphere/ionosphere extension (WACCM-X) (Liu et al., 2018). The analysis of WACCM-X simulation under solar maximum conditions found that the pattern of longitudinal-seasonal variation of PRE displays a remarkable similarity to the pattern of the equatorial plasma bubble (EPB) occurrence rate (Liu, 2020). Moreover, the simulated PRE shows large day-to-day variability, and it is strongly influenced by the variability of both migrating and non-migrating tides.

Vertical  $E \times B$  drifts measured by the Coupled Ion Neutral Dynamics Investigation (CINDI) Ion Velocity Meter (IVM) instrument onboard the Communication/Navigation Outage Forecasting System (C/NOFS), on the other hand, have notable differences from the aforementioned climatology at solstices under solar minimum conditions (Stoneback

et al., 2011): in contrast to the climatological behavior of upward drifts during the day and downward drifts at night (with weak or no of PRE in between), downward drifts in the afternoon and upward drifts near midnight are observed. The upward drifts at night correspond to regions with a high occurrence of post-midnight irregularities during the December 2008 and June 2009 solstices. The apparent semi-diurnal signal was postulated to be related to the semi-diurnal tides in the E-region. However, with semi-diurnal tides present at all seasons and under all solar conditions, it is unclear why this semi-diurnal signature only becomes apparent around solstice especially during Northern summer under solar minimum conditions.

In this study, we will investigate the possible mechanisms that cause upward drift near midnight, and the processes that controls the seasonal and solar cycle variation of the vertical  $E \times B$  drifts using WACCM-X simulations, which reproduce salient features of the variation. Further, an ionospheric electric dynamo model is used to delineate the roles of E and F-region dynamo. A description of the models is given in Section 2. Analysis of model results is presented in Section 3, followed by Conclusions (Section 4).

## 2 Model Description

WACCM-X is one of the atmosphere components of the NCAR Community Earth System Model (CESM) (Hurrell et al., 2013) (also <http://www.cesm.ucar.edu/> for information on the most recent version, CESM version 2), with its top boundary set at the upper thermosphere. Detailed descriptions of the thermospheric and ionospheric physics used in the model can be found in Liu et al. (2010, 2018). The model configuration used in this study is the same as that described by Liu (2020), except that solar minimum condition is used here with the solar radio flux at 10.7 cm (F10.7 flux) set at 70 solar flux unit (sfu,  $10^{-22} \text{ W m}^{-2} \text{ Hz}^{-1}$ ). It is a free running (FR) climate simulation over three model year.

The stand-alone ionospheric electrodynamic introduced by Maute and Richmond (2017) is employed. In the current study, we consider only forcing by the wind dynamo, which are provided by WACCM-X together with the ionospheric conductivities. Compared to the electrodynamic in WACCM-X, the stand-alone dynamo considers the flux tube geometry with the full 3D variation of apex quantities, however the effect on the electric potential solution is small and therefore the  $E \times B$  drift from the stand-alone electrodynamic can be compared to the WACCM-X  $E \times B$  drift.

## 3 Results

From WACCM-X simulations, it is seen that the equatorial vertical  $E \times B$  drift ( $(E \times B)_z$ , referred to as vertical drift hereafter) in June under solar minimum (referred to as  $J_{\min}$  hereafter) conditions display local time (LT)/longitudinal dependence that is different from those in June/solar maximum ( $J_{\max}$ ) and December solar maximum ( $D_{\max}$ ) and solar minimum ( $D_{\min}$ ) (Figure 1). For the specific universal time shown here (UT 20 hour), the  $J_{\min}$  vertical drift becomes downward between LT 16–20 hours (with the largest downward drift of over  $20 \text{ ms}^{-1}$  between 18–19 hour LT/15–30°W), and upward between LT 20 and midnight (with peak value of  $20 \text{ ms}^{-1}$  at  $\sim 22$  hour LT/30°E) (Figure 1(a)). In contrast, the vertical drifts in all the other panels show the typical pre-reversal enhancement (PRE) at 20 hour LT or earlier, followed by a rapid reversal to downward afterward (before 23 hour LT). In the afternoon sector (14–16 hour LT/90–60°W) the equatorial vertical drift in  $J_{\min}$  is upward, switching quickly to downward afterwards. The afternoon equatorial vertical drifts in the other three cases, on the other hand, are weakly upward, straddling upward peaks before and after. Therefore, the equatorial vertical drift for  $J_{\min}$  displays a strong semidiurnal signature, with comparable peak values of  $\sim 20 \text{ ms}^{-1}$  at  $\sim 10$  and 22 hour LT (upward) and  $\sim 1830$  and 5 hour LT (downward). In the

113 other cases, the upward peaks in the morning and around dusk (PRE) are both promi-  
 114 nent, but the downward drift in the afternoon is either very weak or non-existing.

115 The model results, including the vertical drift, show large day-to-day variability  
 116 (Liu, 2020), and the LT/UT and longitude dependence shown in Figures 1 may not be  
 117 the same on different days. So we further examine the monthly climatology of the ver-  
 118 tical drift under solar minimum conditions. Figure 2(a) is the monthly average of the  
 119 vertical drift as a function of longitude and local time for June averaged over three model  
 120 years. The semidiurnal structure is clearly seen in the plot at most longitudes, with lo-  
 121 cal time dependence similar to that from Figure 1(a). Moreover, the longitudinal vari-  
 122 ation is evident in the monthly plot. The specific structure of the longitude variation agree  
 123 with the C/NOFS results (June 2009) (Stoneback et al., 2011, Figure 7) in some longi-  
 124 tude sectors, but not in others. The downward drift between LT 16–20 hour are rather  
 125 strong between 30 and 130°E and 0–30°W and near 0 in the Pacific and American sec-  
 126 tors (180–70°W). These are in general agreement with the C/NOFS results. It then turns  
 127 upward at most longitudes except between 70–110°E (remaining downward) and 150–  
 128 120°W (near 0 LT). By mid-night, the vertical drift becomes 0 or downward at most lon-  
 129 gitudes except between 30–65°E. This strong upward drift around mid-night is compa-  
 130 rable to that in C/NOFS. The monthly average of the vertical drift at local mid-night  
 131 is shown in Figure 2(b) for the whole simulation year under solar minimum conditions.  
 132 It is seen that at midnight the average vertical drift is upward only during northern sum-  
 133 mer months (May–July) between 30–65°E. Three other local maxima are seen at 150°E,  
 134 150°W, and 65°W, with drift values of  $-3 \text{ ms}^{-1}$ , 0 and 0, respectively. This four peak  
 135 structure results from modulation of the dynamo by non-migrating tides diurnal east-  
 136 ward propagating wavenumber 3 (DE3), as determined from a spectral decomposition  
 137 calculation. During northern winter, the monthly average of the vertical drift at mid-  
 138 night is weakly downward with longitudinal variation somewhat similar to that during  
 139 northern summer. It is also noted that although on individual days the vertical drifts  
 140 at midnight generally follow similar longitudinal patterns as the monthly averages, they  
 141 can be upward at multiple longitude locations under solar minimum conditions for both  
 142 June and December (Supporting Information, Figure S1).

143 The semidiurnal signature of the equatorial vertical drift during northern summer  
 144 under solar minimum conditions has been identified by Stoneback et al. (2011) from C/NOFS  
 145 observations. The simulation results discussed above for Jmin, including the local time  
 146 variation with longitudes, compare quite well with the C/NOFS results. As suggested  
 147 by Stoneback et al. (2011), this semidiurnal variation is probably related to semi-diurnal  
 148 tides in the E-region. Since this feature is reproduced in WACCM-X simulations, we will  
 149 examine the model results to understand the connection, especially regarding to the cause  
 150 of the variation with season and solar activities.

151 We then examine the processes that are responsible for the differences between the  
 152 vertical drifts under different solar conditions and at different season as seen above. Here  
 153 we focus on the E to F-region dynamo, in particular the effects of the neutral winds. Specif-  
 154 ically, electric field and  $E \times B$  drifts are calculated using the standalone electrodynamic  
 155 model with neutral winds and ionospheric conductivities input from WACCM-X, and  
 156 UT 20 hour is chosen for detailed analysis. From Figure 3 it is seen that the vertical drifts  
 157 (solid lines) are indeed the same as those from WACCM-X, with the equatorial upward  
 158 drift for Jmin peaking at much later times than those in the Jmax and Dmin cases. In  
 159 the control experiments, only neutral winds in one altitude region are used while winds  
 160 at other altitudes are set to 0 in order to determine their respective contributions to the  
 161 vertical drifts. Specifically, three altitude regions between  $10^{-7}$  hPa,  $1.2 \times 10^{-6}$  hPa,  $1.5 \times 10^{-5}$   
 162 hPa and  $8.5 \times 10^{-5}$  hPa (approximately 250/175/125/105 km respectively for solar min-  
 163 imum, and 330/210/130/105 km respectively for solar maximum) are examined. These  
 164 regions correspond to F-region, upper E-region where SW2 peaks in the winter hemi-  
 165 sphere, and lower E-region where SW2 peaks in the summer hemisphere (Figure 4). It

166 is noted that the drifts from these three regions do not add up to the total drift (solid  
 167 lines in the figure), since contributions above  $10^{-7}$  hPa or below  $8.5 \times 10^{-5}$  are not ac-  
 168 counted for. This decomposition confirms that the dominant role of E-region dynamo  
 169 during the day and F-region dynamo during the night. In all three cases, the vertical drifts  
 170 by the lower E-region dynamo are qualitatively similar: they have an upward peak in  
 171 the morning/noon sector, and become downward between  $\sim 16$  hour and midnight LT  
 172 with the largest values between  $\sim 18$ – $20$  hour LT. This variation is consistent with a pre-  
 173 vious analysis of WACCM-X drift results around dusk (Liu, 2020). Quantitatively, the  
 174 largest change from the upward drift in the morning to the downward drift near dusk  
 175 is found in Jmin. The upward drift in Jmin also peaks earlier (before 10 hour LT) than  
 176 the other two cases.

177 The vertical drift by the F-region dynamo for Jmin, on the other hand, behaves  
 178 differently from the other two cases: the upward drift peaks at  $\sim 21:30$  hour LT and re-  
 179 mains upward till after local midnight, while in the other two cases the upward drifts  
 180 peak at LT 19 hour, and become downward at 22–23 hour LT. Before dusk (LT 16–19  
 181 hour), the vertical drift from the F-region dynamo also shows difference between Jmin  
 182 and the other two: it remains near zero in Jmin but is upward and becomes larger to-  
 183 ward dusk in Jmax/Dmin. Since the downward drift peaks due to E-region dynamo are  
 184 between 18–20 hour LT, the near zero vertical drift before dusk and upward drift peak  
 185 at later local time in Jmin result in a prominent downward drift before 20 hour LT, fol-  
 186 lowed by a large upward peak near 22 hour LT. In the other two cases, the peak down-  
 187 ward and upward drifts occur at similar local times and thus offset each other. It is also  
 188 seen that the upper E-region contributes to the dynamo similarly to the lower E-region  
 189 before dusk and to the F-region after, though with smaller magnitudes. The total ver-  
 190 tical drift in the Jmin case therefore shows an apparent semidiurnal feature, with two  
 191 large upward peaks and two large downward peaks, similar to the observations as reported  
 192 in Stoneback et al. (2011).

193 The seasonal variation and solar cycle dependence of the leading tidal modes, SW2  
 194 and DW1, are then examined. By comparing the zonal wind component of SW2 at F-  
 195 region height ( $5.7 \times 10^{-7}$  hPa) (Figure 4(a) and (b)), it is seen that SW2 attains max-  
 196 imum values ( $\sim 40$   $\text{ms}^{-1}$ ) between June and August (JJA) under solar minimum con-  
 197 ditions. The wave amplitude is the largest in the Southern Hemisphere (SH), but even  
 198 in the Northern Hemisphere it is over  $20$   $\text{ms}^{-1}$ . In contrast, the peak SW2 amplitude  
 199 during JJA under solar maximum conditions is less than  $20$   $\text{ms}^{-1}$ , and at equatorial lat-  
 200 itudes the amplitude is less than  $10$   $\text{ms}^{-1}$ . The SW2 phase (calculated at the equator)  
 201 during JJA under solar minimum conditions approaches 12 hour LT, and the eastward  
 202 wind perturbations are thus strongest approaching noon and midnight. The SW2 phase  
 203 during JJA under solar maximum conditions, on the other hand, is between 6–7 hour and  
 204 18–19 hour LT—almost  $180^\circ$  out of phase with that under solar minimum condition. It  
 205 would be at its strongest westward phase near midnight. It is noted that under solar min-  
 206 imum conditions the SW2 phase also approaches 12 hour LT during northern winter months,  
 207 but the wave amplitude is weaker than during northern summer.

208 DW1 zonal wind component in the F-region also shows different seasonal features  
 209 under different solar conditions (Figure 4(c) and (d)). Under solar minimum conditions,  
 210 the DW1 wave amplitude ( $\sim 40$   $\text{ms}^{-1}$ ) at equatorial latitudes is weak in comparison to  
 211 mid-high latitudes in the summer hemisphere. This is the opposite under solar maximum  
 212 conditions, when the DW1 amplitude is the largest at equatorial latitudes. The DW1  
 213 phase in the equatorial F-region is stable, with that under solar minimum conditions slightly  
 214 later (22 hour LT) than that under solar maximum conditions (21 hour LT). Therefore,  
 215 under solar minimum conditions the zonal wind perturbations of SW2 and DW1 are com-  
 216 parable at equatorial to mid-latitudes, and their superposition results in an enhanced  
 217 eastward wind perturbation near local midnight in the F-region. This is directly respon-  
 218 sible for driving the extended upward  $E \times B$  drift seen in Figure 3(a) for Jmin. The SW2

219 tide does not significantly reinforce the eastward wind in the equatorial F-region in other  
 220 season or under more active solar conditions, because its zonal wind perturbation is weaker  
 221 and/or its phase is opposite (westward) near midnight.

222 To better understand the solar activity dependence of the tidal waves, the latitude/height  
 223 structure of the amplitudes and phases of SW2 and DW1 for Jmin and Jmax are exam-  
 224 ined in Figure 4(e-h). It is clear that these tides transition from propagating modes to  
 225 in-situ forced/trapped modes with increasing altitudes. For the Jmin SW2, it shows phase  
 226 propagation above  $\sim 330$  km ( $\sim 10^{-8}$  hPa) over the Southern (winter) hemisphere and  
 227 northern equatorial latitudes, while Jmax SW2 phase stagnates at  $\sim 300$  km ( $2 \times 10^{-7}$   
 228 hPa). Consequently, the SW2 amplitude at the F-region altitudes is much larger in the  
 229 case of Jmin as seen in Figure 4. The phase progression of DW1 in Jmin also extends  
 230 to higher altitudes ( $\sim 250$  km,  $10^{-7}$  hPa) than Jmax ( $\sim 220$  km,  $10^{-6}$  hPa), but the F-  
 231 region wind is generally dominated by the in-situ forced DW1 winds, especially under  
 232 solar maximum conditions and at equatorial latitudes and summer high latitudes (also  
 233 seen in Figure 4). It is therefore evident that SW2 can significantly modulate the F-  
 234 region wind under solar minimum conditions, but not so much under solar maximum con-  
 235 ditions. This is also clearly seen from the total zonal wind at the equator (Supporting  
 236 Information Figure S2).

## 237 4 Conclusions

238 Our analysis suggests that the E-region wind dynamo have similar contributions  
 239 under different solar cycle conditions, and the interplay of the dominant migrating tides,  
 240 DW1 and SW2, determines the F-region wind dynamo and the solar cycle variation of  
 241 the equatorial  $E \times B$  drift. Under solar minimum conditions, the SW2 tide propagate to  
 242 and beyond the F-region in the winter hemisphere, and consequently its zonal wind am-  
 243 plitude in the F-region is much stronger than that under solar maximum conditions. The  
 244 zonal wind DW1 in the F-region, on the other hand, comes mostly from in-situ forcing  
 245 under both solar maximum and minimum conditions, but with much larger amplitude  
 246 at low latitudes for the former. Consequently, the SW2 tidal modulation of the F-region  
 247 wind is more significant under solar minimum conditions. Moreover, the SW2 zonal wind  
 248 phase at F-region height also shows a solar cycle dependence:  $\sim 12$  hour LT during so-  
 249 lar minimum and  $\sim 6$  hour LT during solar maximum. The superposition of DW1 and  
 250 SW2 results in a strong eastward wind perturbation near local midnight, and a westward  
 251 (or weakly eastward) wind around dusk in the F-region under solar minimum conditions.  
 252 This in turn drives a F-region dynamo with an equatorial upward drift between 18 and  
 253 01 hour local time, reaching its maximum near 22 hour LT. In contrast, the F-region wind  
 254 is dominated by DW1 during solar maximum (eastward between 16 and 4 hour LT), and  
 255 the SW2 modulation is rather insignificant. This drives an equatorial upward drift within  
 256 the local time range 07 to 23 hour LT, with peak values near 19 hour. The total equa-  
 257 torial vertical  $E \times B$  drift during solar minimum is downward in the local afternoon and  
 258 dusk, followed by an upward drift that extends toward midnight. Therefore, the appar-  
 259 ent semi-diurnal variation during solar minimum is not a direct manifestation of SW2  
 260 in the E-region: The upward peaks in the local morning and pre-midnight are driven mainly  
 261 by the E-region wind and the F-region wind respectively, and the downward peaks near  
 262 the dusk peak and post midnight/early morning are by E-region and F-region winds re-  
 263 spectively.

264 Longitudinal variation is apparent in both observations (Stoneback et al., 2011) and  
 265 modeling results presented here. The 4-peak structure as seen in Figure 2 suggests the  
 266 modulation by non-migrating tides, which is known to cause longitudinal variation (e.g.  
 267 Fang et al., 2013). Modulation by the geometry and strength of geomagnetic field is an-  
 268 other cause of longitudinal variation (e.g. Fang et al., 2012). The detailed mechanism  
 269 responsible for the longitudinal variation of the nighttime vertical drift, including the  
 270 upward drift at midnight at specific longitude sectors, needs to be further elucidated in

271 future studies. Moreover, there is an apparent difference between the equatorial upward  
272 drift at June and December solstices under solar minimum conditions, with the semid-  
273 iurnal feature and the upward drift around midnight more pronounced in the former case.  
274 In the model, this difference stems from the different semi-diurnal tidal winds at the F-  
275 region height, with the winter hemisphere wave amplitude much stronger around June  
276 solstice. The cause of this hemispheric difference in SW2 in the thermosphere should be  
277 further examined in future studies.

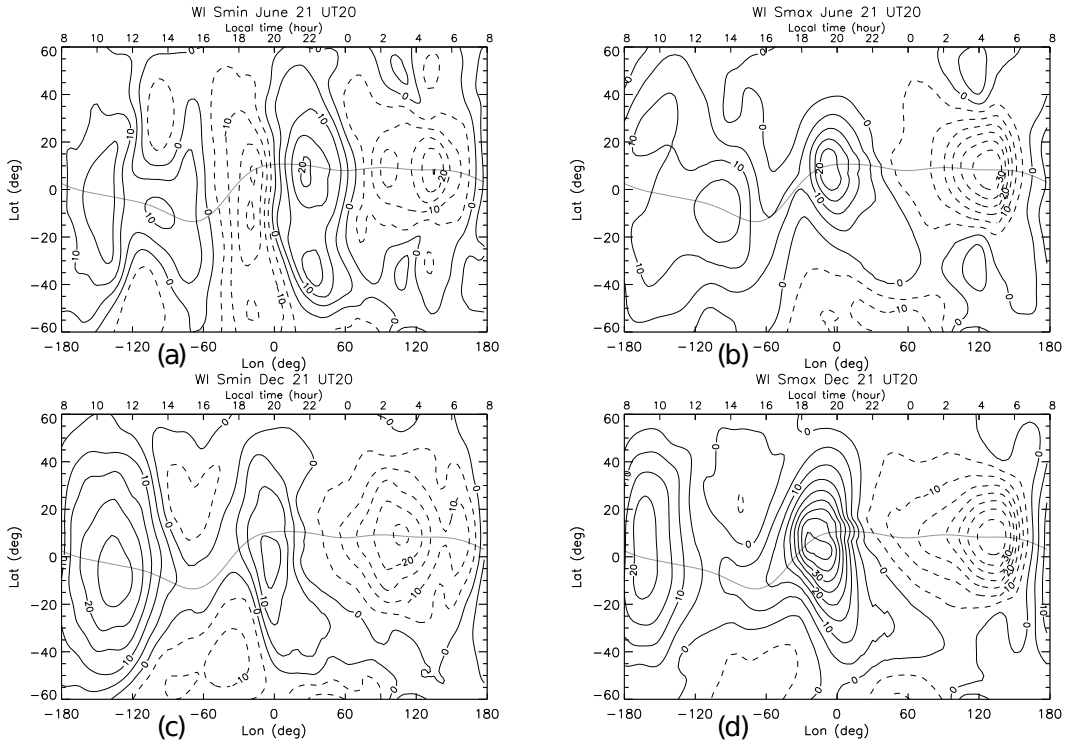


Figure 1: The vertical  $E \times B$  drift (WI in figure) on June 21 (upper panel) and December 21 (lower panel) at 20 hour UT under solar minimum (left panel) and solar maximum (right panel) conditions. The local times are marked on the upper x axis. Contour interval:  $5 \text{ ms}^{-1}$  (solid: upward). Thin grey line: The magnetic equator.

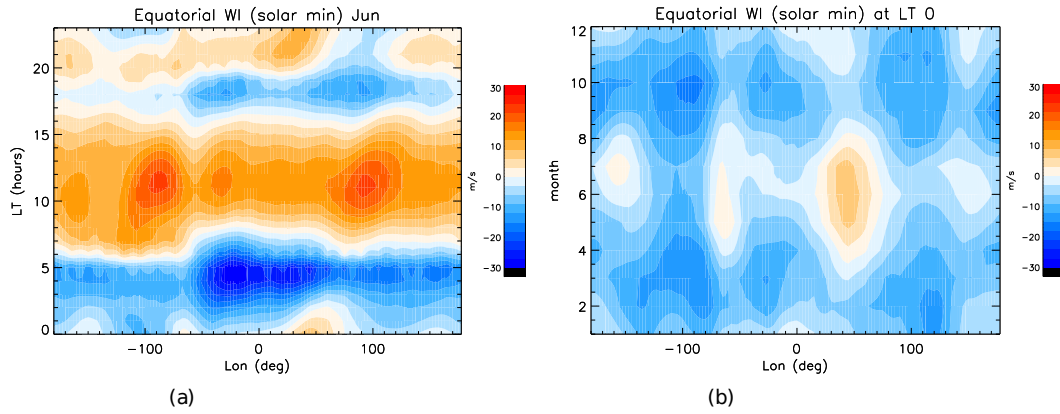


Figure 2: Monthly averaged vertical  $E \times B$  drift (a) for June over all local times, and (b) for 0 hour local time over all year under solar minimum conditions.

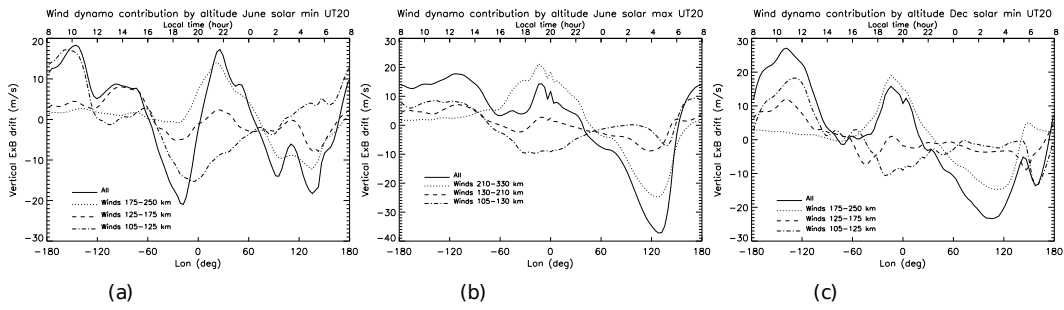


Figure 3: Contribution to total equatorial vertical  $E \times B$  drift by different altitude regions for (a) June, solar minimum, (b) June, solar maximum and (c) December, solar minimum. 20 hour UT is shown, and the local times are marked by the upper x-axis.

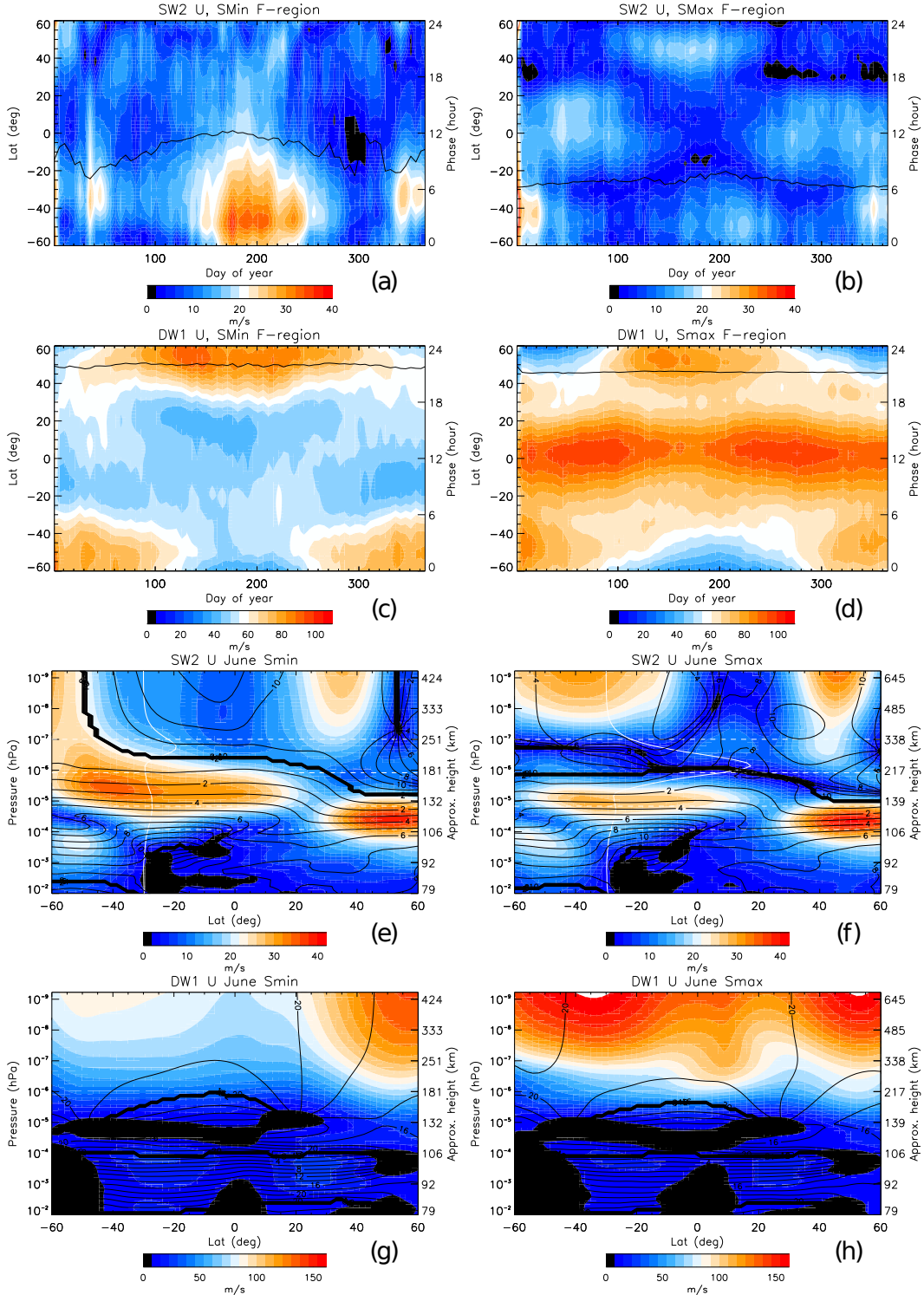


Figure 4: Seasonal variation of SW2 zonal wind amplitude (color contour) and phase (black line) in the F-region ( $5.7 \times 10^{-7}$  hPa) for (a) solar minimum and (b) solar maximum. (c-d): Similar to (a-b) but for DW1. In (a-d) the phase values (marked by the y-axis on the right side) are in terms of local times for the respective tidal components at the equator. The latitude-height structure of the amplitude (color contour) and phase (line contour) of SW2 zonal wind for June under (e) solar minimum and (f) solar maximum conditions. (g-h): Similar to (e-f) but for DW1. The contour line interval is 1 hour in (e-f) and 2 hours in (g-h). The vertical profiles of Pedersen conductivity at  $30^\circ\text{S}$  are plotted in e (solar minimum) and f (solar maximum), with their zero values at  $30^\circ\text{S}$  and the conductivity values can be read from the x-axis (unit:  $10^{-6} \text{ Sm}^{-1}$ ). The horizontal dashed lines are at  $10^{-7}$  hPa,  $1.2 \times 10^{-6}$  hPa,  $1.5 \times 10^{-5}$  hPa and  $8.5 \times 10^{-5}$  hPa pressure levels.

## Open Research

NCAR CESM/WACCM is an open-source community model, and is available at <https://doi.org/10.5065/D67H1H0V>. Model output used for this study is available through GLOBUS (shared end point: <https://tinyurl.com/mv2e6e2u>). Registration for a free Globus account is required to connect through the endpoint.

## Acknowledgments

HLL acknowledges partial support by NASA Grants 80NSSC20K1323, 80NSSC20K0601, 80NSSC20K0633, 80NSSC21K1305, 80NSSC20K0189, 80NSSC22K1018, and 80NSSC22M0163. AM is supported by NASA awards 80NSSC23K1123, 80NSSC20K1784, and 80MSFC20D0004. National Center for Atmospheric Research is a major facility sponsored by the National Science Foundation under Cooperative Agreement No. 1852977.

## References

- Anderson, D. N., Reinisch, B., Valladares, C. E., Chau, J., & Veliz, O. (2004). Forecasting the occurrence of ionospheric scintillation activity in the equatorial ionosphere on day-to-day basis. *J. Atmos. Sol-Terr Phys.*, *66*, 1567-1572.
- Fang, T.-W., Akmaev, R., Fuller-Rowell, T., Wu, F., Maruyama, N., & Millward, G. (2013). Longitudinal and day-to-day variability in the ionosphere from lower atmosphere tidal forcing. *Geophysical Research Letters*, *40*, 2523–2528. doi: 10.1002/grl.50550
- Fang, T.-W., Fuller-Rowell, T., Akmaev, R., Wu, F., Wang, H., & Anderson, D. (2012). Longitudinal variation of ionospheric vertical drifts during the 2009 sudden stratospheric warming. *Journal of Geophysical Research: Space Physics*, *117*. doi: 10.1029/2011JA017348
- Farley, D. T., Bonelli, E., Fejer, B. G., & Larsen, M. F. (1986). The prereversal enhancement of the zonal electric field in the equatorial ionosphere. *Journal of Geophysical Research*, *91*, 13723–13728.
- Fejer, B. G., Scherliess, L., & de Paula, E. R. (1999). Effects of the vertical plasma drift velocity on the generation and evolution of equatorial spread F. *Journal of Geophysical Research*, *104*, 19859-19869.
- Fesen, C. G., Crowley, G., Roble, R. G., Richmond, A. D., & Fejer, B. G. (2000). Simulation of the pre-reversal enhancement in the low latitude vertical ion drift. *Geophysical Research Letters*, *27*, 1851-1854.
- Huang, C.-S. (2018, Jan 09). Effects of the postsunset vertical plasma drift on the generation of equatorial spread f. *Progress in Earth and Planetary Science*, *5*. doi: 10.1186/s40645-017-0155-4
- Huang, C.-S., & Hairston, M. R. (2015). The postsunset vertical plasma drift and its effects on the generation of equatorial plasma bubbles observed by the c/nofs satellite. *Journal of Geophysical Research: Space Physics*, *120*, 2263–2275. (2014JA020735) doi: 10.1002/2014JA020735
- Hurrell, J. W., Holland, M. M., Gent, P. R., Ghan, S., Kay, J. E., Kushner, P. J., ... Marshall, S. (2013). The community earth system model: A framework for collaborative research. *Bulletin of the American Meteorological Society*, *94*, 1339-1360. doi: 10.1175/BAMS-D-12-00121.1
- Kil, H., Paxton, L. J., & Oh, S.-J. (2009). Global bubble distribution seen from ROCSAT-1 and its association with the evening prereversal enhancement. *Journal of Geophysical Research: Space Physics*, *114*. (A06307) doi: 10.1029/2008JA013672
- Liu, H.-L. (2020). Day-to-day variability of pre-reversal enhancement in the vertical ion drift in response to large-scale forcing from the lower atmosphere. *Space Weather*, *18*, e2019SW002334. doi: 10.1029/2019SW002334

- 328 Liu, H.-L., Bardeen, C. G., Foster, B. T., Lauritzen, P., Liu, J., Lu, G., . . . Wang,  
329 W. (2018). Development and validation of the whole atmosphere commu-  
330 nity climate model with thermosphere and ionosphere extension (waccm-x  
331 2.0). *Journal of Advances in Modeling Earth Systems*, *10*, 381-402. doi:  
332 10.1002/2017MS001232
- 333 Liu, H.-L., Foster, B. T., Hagan, M. E., McInerney, J. M., Maute, A., Qian, L., . . .  
334 Oberheide, J. (2010). Thermosphere extension of the Whole Atmosphere  
335 Community Climate Model. *Journal of Geophysical Research*, *115*. doi:  
336 10.1029/2010JA015586
- 337 Maute, A., & Richmond, A. (2017). F-region dynamo simulations at low and mid-  
338 latitude. *Space Science Reviews*, *206*, 471-493. doi: 10.1007/s11214-016-0262  
339 -3
- 340 Scherliess, L., & Fejer, B. G. (1999). Radar and satellite global equatorial f region  
341 vertical drift model. *Journal of Geophysical Research*, *104*, 6829-6842.
- 342 Stoneback, R. A., Heelis, R. A., Burrell, A. G., Coley, W. R., Fejer, B. G., &  
343 Pacheco, E. (2011). Observations of quiet time vertical ion drift in the  
344 equatorial ionosphere during the solar minimum period of 2009. *Journal of*  
345 *Geophysical Research*, *116*. doi: doi:10.1029/2011JA016712
- 346 Tsunoda, R. T. (1985). Control of the seasonal and longitudinal occurrence of equa-  
347 torial scintillations by the longitudinal gradient in integrated e region pedersen  
348 conductivity. *Journal of Geophysical Research*, *90*, 447-456.